






Article

Electrochemical Performance of Potassium Hydroxide and Ammonia Activated Porous Nitrogen-Doped Carbon in Sodium-Ion Batteries and Supercapacitors

Yuliya V. Fedoseeva ^{1,*}, Elena V. Shlyakhova ¹, Svetlana G. Stolyarova ¹, Anna A. Vorfolomeeva ¹, Alina D. Nishchakova ¹, Mariya A. Grebenkina ¹, Anna A. Makarova ², Konstantin A. Kovalenko ¹, Alexander V. Okotrub ¹ and Lyubov G. Bulusheva ^{1,*}

¹ Nikolaev Institute of Inorganic Chemistry SB RAS, 3 Acad. Lavrentiev Ave., 630090 Novosibirsk, Russia

² Physical Chemistry, Institute of Chemistry and Biochemistry, Free University of Berlin, 14195 Berlin, Germany

* Correspondence: fedoseeva@niic.nsc.ru (Y.V.F.); bul@niic.nsc.ru (L.G.B.); Tel.: +7-3833305352 (Y.V.F. & L.G.B.)

Abstract: Carbon nanomaterials possessing a high specific surface area, electrical conductivity and chemical stability are promising electrode materials for alkali metal-ion batteries and supercapacitors. In this work, we study nitrogen-doped carbon (NC) obtained by chemical vapor deposition of acetonitrile over the pyrolysis product of calcium tartrate, and activated with a potassium hydroxide melt followed by hydrothermal treatment in an aqueous ammonia solution. Such a two-stage chemical modification leads to an increase in the specific surface area up to 1180 m² g⁻¹, due to the formation of nanopores 0.6–1.5 nm in size. According to a spectroscopic study, the pore edges are decorated with imine, amine, and amide groups. In sodium-ion batteries, the modified material mNC exhibits a stable reversible gravimetric capacity in the range of 252–160 mA h g⁻¹ at current densities of 0.05–1.00 A g⁻¹, which is higher than the corresponding capacity of 142–96 mA h g⁻¹ for the initial NC sample. In supercapacitors, the mNC demonstrates the highest specific capacitance of 172 F g⁻¹ and 151 F g⁻¹ at 2 V s⁻¹ in 1 M H₂SO₄ and 6 M KOH electrolytes, respectively. The improvement in the electrochemical performance of mNC is explained by the cumulative contribution of a developed pore structure, which ensures rapid diffusion of ions, and the presence of imine, amine, and amide groups, which enhance binding with sodium ions and react with protons or hydroxyl ions. These findings indicate that hydrogenated nitrogen functional groups grafted to the edges of graphitic domains are responsible for Na⁺ ion storage sites and surface redox reactions in acidic and alkaline electrolytes, making modified carbon a promising electrode material for electrochemical applications.

Keywords: N-doped porous carbon; potassium hydroxide melt treatment; ammonia treatment; Na-ion batteries; supercapacitors



Citation: Fedoseeva, Y.V.; Shlyakhova, E.V.; Stolyarova, S.G.; Vorfolomeeva, A.A.; Nishchakova, A.D.; Grebenkina, M.A.; Makarova, A.A.; Kovalenko, K.A.; Okotrub, A.V.; Bulusheva, L.G. Electrochemical Performance of Potassium Hydroxide and Ammonia Activated Porous Nitrogen-Doped Carbon in Sodium-Ion Batteries and Supercapacitors. *Inorganics* **2022**, *10*, 198. <https://doi.org/10.3390/inorganics10110198>

Academic Editors: Faxing Wang and Tao Wang

Received: 5 October 2022

Accepted: 1 November 2022

Published: 7 November 2022

Publisher's Note: MDPI stays neutral with regard to jurisdictional claims in published maps and institutional affiliations.



Copyright: © 2022 by the authors. Licensee MDPI, Basel, Switzerland. This article is an open access article distributed under the terms and conditions of the Creative Commons Attribution (CC BY) license (<https://creativecommons.org/licenses/by/4.0/>).

1. Introduction

The development of new technologies for electrochemical energy storage devices with high energy density and high power density is essential for portable electronics and electrical vehicles. Recently, sodium-based technologies have become the subject of intense research due to the inexhaustibility of resources and the cheapness of Na. Sodium-ion batteries (SIBs) operate similar to lithium-ion batteries, and are generally assessed as being the most promising candidates for alternative energy storage technologies. Carbonaceous materials are attracting a lot of attention and are considered as potential anode materials for SIBs due to their high conductivity, excellent mechanical and thermal stability, and an abundance of active sodium storage sites [1]. However, the large size of the Na⁺ ions and its weak interaction with graphitic layers complicates the intercalation of sodium into the graphite structure [2]. It has been recently established, that Na⁺ adsorption on the surface of nongraphitic carbon electrodes is the main mechanism of sodium storage for these materials [3]. The insertion of Na⁺ ions into the expanded interlayer space and into

pores also occurs in carbon-based electrodes [4,5]. Thus, the hierarchical porous structure and large available surface area with defects and functional groups can provide rich sites that are active for sodium storage and are characterized by strong binding energy and a high energy storage potential. Nowadays, the most desirable carbon anode materials are heteroatom-doped sp^2 -carbons with a highly developed porous structure and a stable framework, including hard and soft carbon, plant-derived and template carbon [6–11]. They are easy to prepare and have a relatively low cost [12–14]. Doping of carbon materials with nitrogen is an affordable and promising approach for introducing a large number of defects that are attractive for sodium adsorption and sodium penetration into the volume of a carbon electrode [15–17]. In addition, graphitic nitrogen improves electrical conductivity of carbon materials due to its extra valence electron [18,19].

Conventional nitrogen-doping methods, including pyrolysis of nitrogen-containing carbon sources or treatment with nitrogen plasma, yield three main forms of nitrogen dopants (pyridinic, pyrrolic, and graphitic (or quaternary) [20–24], the significance of which in electrochemical applications has been widely studied [23–25]. Density functional theory (DFT) calculations revealed that the edge nitrogen species are more attractive for Na^+ ions [26]. Numerous experimental and theoretical studies have demonstrated that pyridinic nitrogen, located at the edges of graphitic domains or atomic vacancies, is clearly a favorable site for the chemisorption of lithium and sodium ions [18,27].

The role of other forms of nitrogen, such as imine, amine, and amide groups, is rarely considered in the electrochemical performance of carbon nanomaterials. Only several papers report on the effect of hydrogenated nitrogen species on the ability of carbon materials to accumulate alkali metal ions [28–31]. Amine-functionalized carbon nanosheets have demonstrated exceptional efficiency in SIBs in the low potential region, which was associated with redox processes involving surface amino groups [28]. Zhundong coal activated in an ammonia atmosphere showed an increased specific capacity of 200 mA h g^{-1} at a current density of 200 mA g^{-1} , even after 500 cycles for SIBs [29]. The role of imine nitrogen to enhance Li and Na storage performance was demonstrated for the nitrogen doped γ -graphyne [30].

Chemical activation with potassium hydroxide is a common method for modifying carbon materials as it increases their porosity and surface area, which are necessary for good electrochemical performance [15,32–34]. Moreover, KOH activation changes the chemical state of the carbon surface and increases the content of oxygen-containing groups, mainly hydroxyl groups. DFT calculations revealed that the presence of dangling carbon bonds and some oxygen-containing functional groups at the edges of atomic vacancies enhances Na binding as compared to nonmodified graphene [35]. However, in the case of nitrogen-containing carbon samples, a strong decrease in the nitrogen content was observed as a result of KOH modification [36]. An ammonia solution can be used as a reagent for the introduction of nitrogen functional groups by impregnation, since ammonium ions formed in aqueous media interact with functional groups on chemically activated carbon [37,38]. The electrochemical reactions of some nitrogen- and oxygen-functional edge groups can be applied to various alkali metal-ion batteries, making chemically modified carbon very attractive as universal electrodes [39].

The ammonia-assisted hydrothermal method offers simplicity and mild reaction conditions. According to previously published results, carbon nanomaterials after hydrothermal treatment with ammonia have a high specific surface area and pore volume, and the reaction of ammonia with the edges of graphene domains leads to the replacement of some oxygen-containing groups by nitrogen species [40–43]. It was found that pyridinic N, hydrogenated pyridinic N, graphitic N, amine and amide groups can be successfully introduced into the carbon materials due to the reaction with ammonia in hydrothermal conditions [40–43]. For carbon nanomaterials with abundant vacancy defects and oxygen-containing groups, interaction with ammonia can result in the development of NH_x groups. However, little attention is paid to the effect of successive treatment with KOH and an ammonia solution on

the composition of the functional groups of a carbon nanomaterial and its electrochemical performance in SIBs [44].

Therefore, the goal of our research was to synthesize porous N-doped carbon (NC)-containing NH_x groups in order to study their effect on the Na^+ ion storage. In addition, the original NC and the modified NC (mNC) were tested in aqueous electrolytes of supercapacitors (SCs), where the electrostatic charge accumulates at the electrode–electrolyte interface and strongly depends on the surface area and porosity of the electrode material. The second charge storage mechanism in SCs is based on pseudocapacitance, introduced by fast and reversible Faradaic processes occurring due to electroactive functional groups. In particular, nitrogen- and oxygen-containing species can participate in electrochemical reactions with H^+ and OH^- ions [45]. Porous NC materials obtained from melanin and polydopamine [46] or using various nitrogen-containing compounds (NH_4Cl , $(\text{NH}_4)_2\text{CO}_3$, urea, etc. [47,48]) as activating agents demonstrated excellent electrochemical properties in SCs due to their high electrical conductivity, good wettability, suitable pore size distribution, and additional pseudocapacitance effect. In addition, modified carbon can be used as a conductive additive into an insulating polymer matrix to form cross-linked networks; such composite hydrogels exhibit excellent electrochemical properties and mechanical stability and can be used as flexible electrodes in SCs [49]. Our studies show that the modification of NC with a KOH melt followed by hydrothermal treatment with ammonia is a simple low-cost way for improving the electrochemical performance of porous NC in SIBs and SCs.

2. Results

2.1. Structural Aspects

The modification procedure used is schematically shown in Figure 1a. The starting NC was obtained by chemical vapor deposition (CVD) of acetonitrile on a template, formed as a result of the thermal decomposition of calcium tartrate [43,50]. Such NC has a spongy morphology and consists of graphitic layers of 10 nm thick, forming a framework with pores in the range of 0.6–30 nm. The increase in the porosity and the introduction of NH_x species were carried out by a two-stage modification of NC with a potassium hydroxide melt at a temperature of 750 °C for 2 h, and then with an aqueous solution of ammonia under hydrothermal conditions at a temperature of 147 °C for 30 h (mNC sample).

The Raman scattering spectra of NC and mNC exhibit a sharp G band at 1586 cm^{-1} and a broad D band at 1354 cm^{-1} (Figure 1b). These bands correspond to the E_{2g} mode in sp^2 -hybridized carbon rings and chains and the A_{1g} breathing mode in rings, respectively [51]. A broad peak at around 2800 cm^{-1} is attributed to the two-phonon (2D) Raman scattering in graphene layers. The high intensity of the D band indicates the small size of graphitic domains and the presence of defects and disorders in the graphitic structure. The intensity ratio of the D and G bands ($I_D:I_G$) is used to assess the defectiveness of the graphitic material. The $I_D:I_G$ ratio increases from 0.90 for NC to 0.93 for mNC, which indicates a decrease in the size of defect-free graphitic domains after the modification procedure.

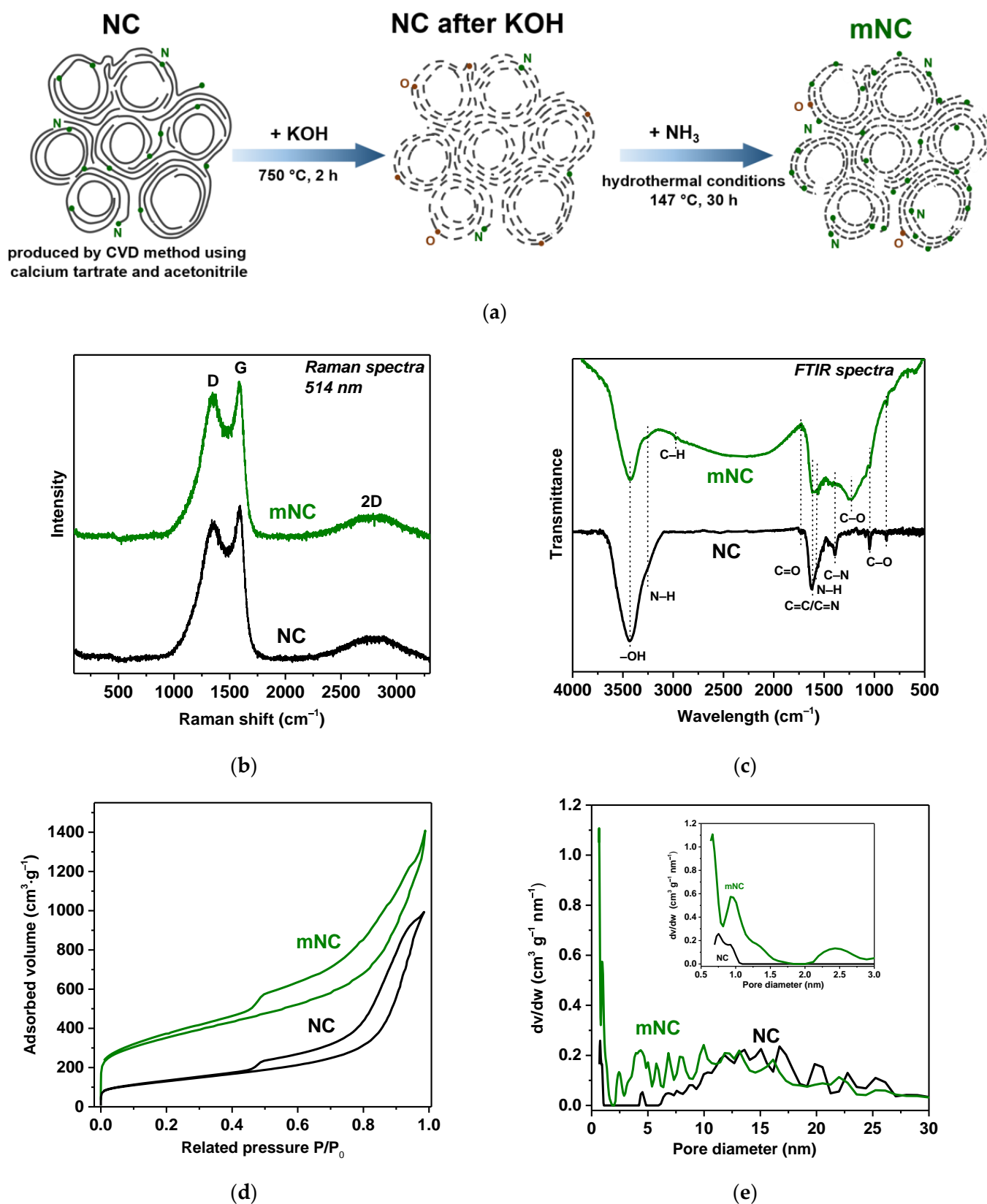


Figure 1. (a) Schematic illustration of mNC preparation; (b) Raman and (c) FTIR spectra, (d) adsorption–desorption isotherms of N₂ at 77 K and (e) DFT pore size distributions in NC and mNC samples. The inset shows the pore size distribution in the range of 0.5–3.0 nm.

Figure 1c compares the Fourier transform infrared (FTIR) spectra of the initial NC sample and the modified mNC sample. The former spectrum identifies hydroxyl O–H stretching vibrations at 3400 cm^{-1} , N–H stretching vibrations at 3262 cm^{-1} , C=O stretching vibrations at 1740 cm^{-1} , C=C/C=N/C=O stretching vibrations in aromatic rings at $1580\text{--}1620\text{ cm}^{-1}$, aromatic amine C=N stretching vibrations at 1391 cm^{-1} , and C–O stretching vibrations at 1049 cm^{-1} [43,52,53]. The FTIR spectrum of mNC shows changes in functional groups after modification procedures. The bands corresponding to hydroxyl –OH (3400 cm^{-1}) and C–O (1049 cm^{-1}) groups become weaker. The featureless band which appeared in the range of $2000\text{--}3000\text{ cm}^{-1}$ can be attributed to $\text{N}^+\text{--H}$ stretching vibrations from ammonia cations chemisorbed on the hydroxyl groups. These chemisorbed species are probably only present in the fresh sample. The spectrum of mNC shows the absence of a band at 1740 cm^{-1} from C=O groups, and the appearance of a band at a lower frequency of $\sim 1600\text{ cm}^{-1}$ assigned to the C–N stretching and N–H bending vibrations in primary amines and amides [54–57]. The broad band observed in the mNC spectrum at 1230 cm^{-1} is due to the stretching vibrations of phenol C–O or acyl C=O groups, and a weak band at 2970 cm^{-1} reflects the stretching vibrations of C–H bonds. These results indicate the presence of amine, amide, and phenol groups on the surface of mNC.

Figure 1d presents the adsorption–desorption isotherms of N_2 measured at 77 K for NC and mNC samples. The isotherms are of type II, characterizing unlimited monolayer-multilayer adsorption of gases on nonporous or macroporous materials. However, there is a hysteresis loop, associated with the secondary process of capillary condensation leading to complete filling of the mesopores. The inflection point at the lowest $P/P_0 \sim 0$ corresponds to the filling of micropores. According to the Brunauer–Emmett–Teller (BET) theory, the specific surface area is $440\text{ m}^2\text{ g}^{-1}$ for NC and $1180\text{ m}^2\text{ g}^{-1}$ for mNC. It should be noted that the specific surface area of NC after the first stage of the modification with KOH only increases to $711\text{ m}^2\text{ g}^{-1}$ (Figure S1a).

The total pore volume and pore size distribution are calculated using DFT. The pore volume is $1.4\text{ cm}^3\text{ g}^{-1}$ for NC and increases to $1.8\text{ cm}^3\text{ g}^{-1}$ for mNC. Figure 1e shows the plots of pore size distribution in NC and mNC. It can be seen that the initial material mainly contains mesopores with sizes in the range of 4–27 nm, and a small amount of micropores with sizes less than 1 nm (inset in Figure 1e). However, mNC contains a greater number of small mesopores 2 to 10 nm in size and micropores 0.6 to 1.5 nm in size, which reduces the average pore diameter of the modified sample. The volume of micropores smaller than 2 nm is $0.2\text{ cm}^3\text{ g}^{-1}$ and they provide $506\text{ m}^2\text{ g}^{-1}$ of the specific surface area of mNC. The volume and area of mesopores are $1.6\text{ cm}^3\text{ g}^{-1}$ and $674\text{ m}^2\text{ g}^{-1}$, respectively, and exceed the corresponding values of micropores. It should be noted that changes in the pore structure are caused by both modification procedures, not only by KOH activation (Figure S1b).

Figure 2 shows data from X-ray photoelectron spectroscopy (XPS), a surface-sensitive quantitative method. The survey spectra of NC and mNC (Figure 2a) contain signals of carbon, nitrogen, and oxygen. The total nitrogen content decreases from 6 at% in NC up to 4 at% in mNC. Note, that the first treatment with KOH causes the nitrogen content drop to 1 at% (Figure S2a). Therefore, subsequent treatment with ammonia partially compensates for this loss of nitrogen. The oxygen content does not change after the two-stage modification.

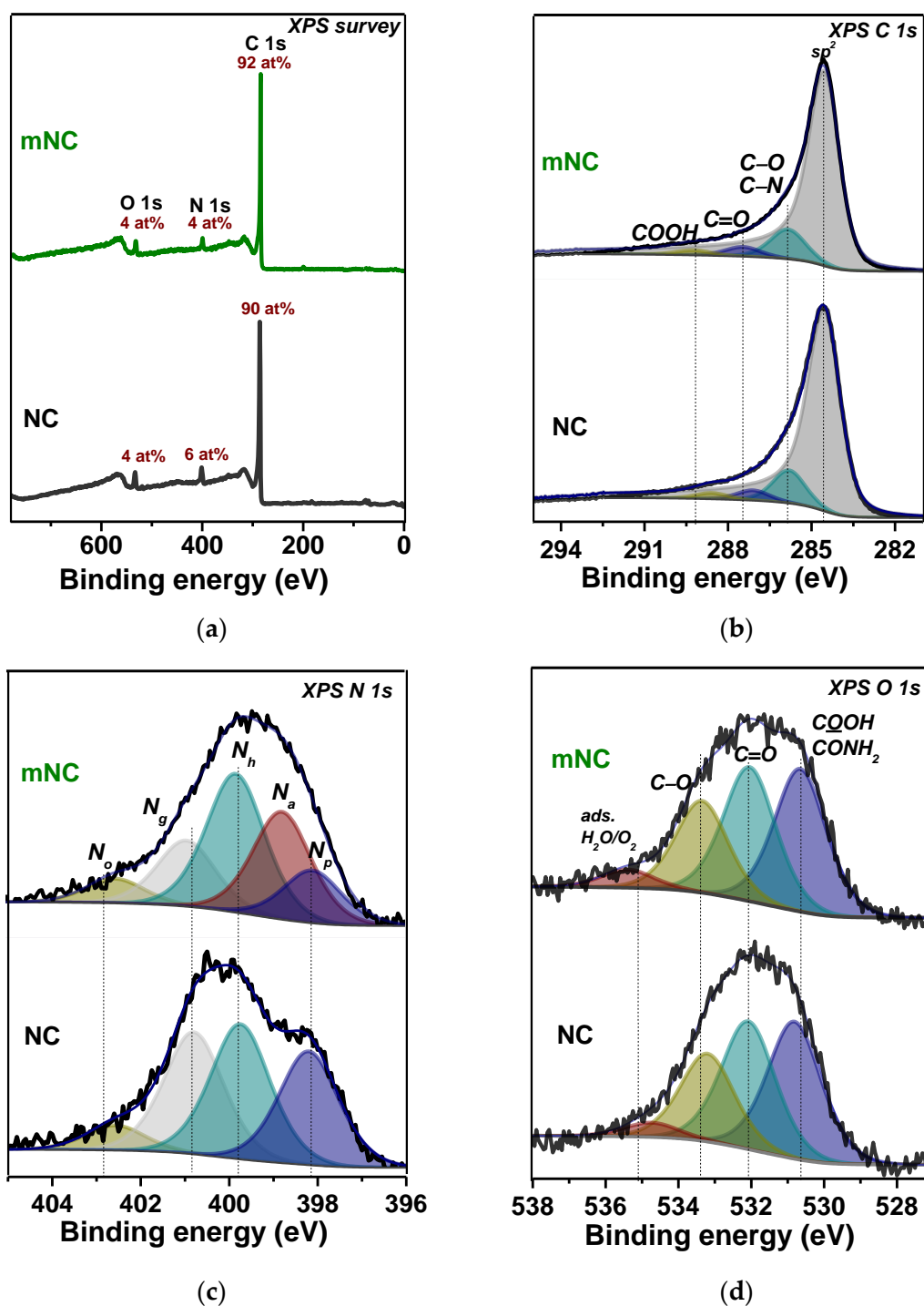


Figure 2. XPS (a) survey, (b) C 1s, (c) N 1s and (d) O 1s spectra of NC and mNC.

The C 1s spectra of NC and mNC contain four components (Figure 2b) originating from sp^2 -carbon (284.5 eV), defect states and carbon bonded with oxygen or nitrogen (286.0 eV), carbon double-bonded with oxygen (287.3 eV), and carboxylic carbon (288.5 eV). The components have similar energy position, width, and area in both spectra. The N 1s spectra of NC and mNC are approximated by four or five components of the same width, as shown in Figure 2c. Four nitrogen forms are found in the initial sample NC: pyridinic N at 398.1 eV (N_p), hydrogenated pyridinic N at 399.8 eV (N_h), graphitic N at 400.9 eV (N_g), and oxidized nitrogen species at 402.7 eV (N_o) [58]. The ratio of $N_p:N_h:N_g:N_o$ is 1:1:1:0.2. The N 1s spectrum of mNC contains the above components and a new component (N_a)

at 398.8 eV. Since KOH treatment removes most of the nitrogen dopants from the NC's surface, leaving the residual N_0 state (Figure S2c); almost all forms of nitrogen found in the mNC sample are most likely formed due to interaction with an aqueous ammonia solution in the second stage of modification. Nitrogen can be introduced as pyridinic N, pyrrolic N or hydrogenated pyridinic N into the aromatic rings or as NH_x groups (imine, amine or amide), bonded directly to the edges of aromatic rings at defect sites, that form as a result of KOH etching [43,59,60]. The reaction of ammonia with the edges of defects can produce primary amine groups ($-NH_2$), while ammonia reacts with carbonyl and carboxyl groups to form imine ($=N-H$) and amide ($-C(O)NH_2$) groups through nucleophilic substitution reaction [61]. According to the reported data, the intense component N_h at 399.8 eV can refer to amine or amide groups [28,61,62], while the component N_a at 398.8 eV arises from imine groups [63,64]. The XPS O 1s spectra of the samples show four peaks of the same area and width as oxygen double-bonded with carbon ($C=O$) in the carboxyl (530.8 eV) and carbonyl groups (532.1 eV), oxygen single-bonded to a carbon atom ($C-O$, 533.3 eV), and oxygen from adsorbed H_2O or O_2 (535.2 eV). Changes in the spectral profile of the O 1s line are not visible after the two-stage chemical modification of NC, but according to the FTIR spectrum of mNC (Figure 1c), components at 533.3 eV and 530.8 eV can more likely be attributed to phenol oxygen [65] and oxygen in $-C(O)NH_2$, respectively.

Near-edge X-ray absorption fine structure (NEXAFS) spectroscopy reflects the unoccupied density of electronic states and is used to gain additional information about elements. The NEXAFS C K- and N K-edge spectra of NC and mNC are presented in Figure 3. The main peaks of the C K-edge spectra located at 285.4 eV and 288.5 eV correspond to transitions of core electrons onto the antibonding π^* and σ^* $C=C$ sp^2 states, respectively. The presence of intense narrow π^* -peaks in the spectra of both samples reflects the graphite-like structure of carbon shells in as-grown NC, and its retention after modification. Peak F at 288.0 eV, corresponding to carbon atoms connected with oxygen- or hydrogen- or nitrogen-containing groups ($\pi^* C=O$, $\sigma^* C-H$, and $\sigma^* C-N$ states) [66,67], has a low intensity in the spectrum of NC. For mNC, the intensity of the peak F increases due to the attachment of extra functional groups during modification. Moreover, the asymmetric line shape of the π^* -peak in the spectrum of mNC confirms the embedding of oxygen or nitrogen into aromatic rings [68].

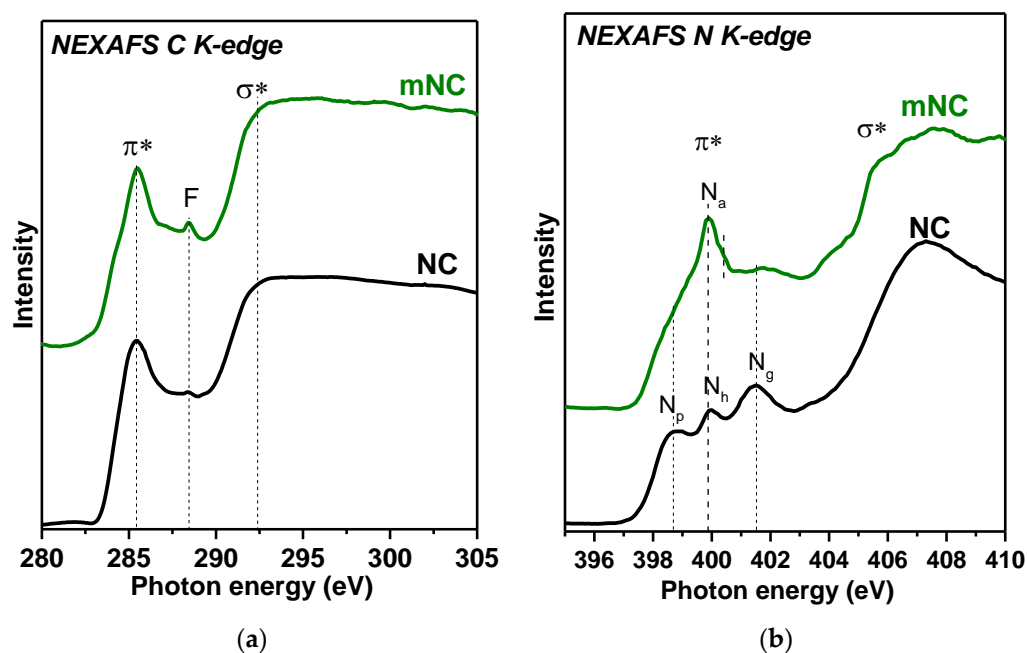


Figure 3. NEXAFS (a) C K-edge and (b) N K-edge spectra of NC and mNC samples.

The NEXAFS N K-edge spectrum of NC shows a series of peaks in the energy range from 398.0 to 403.0 eV attributed to $1s \rightarrow \pi^*$ electron transitions, and a broad spectral feature at energies above 405.0 eV due to $1s \rightarrow \sigma^*$ electron transitions. The energy position of the three π^* peaks reveals the presence of N_p (398.7 eV), N_h (399.9 eV) and N_g (400.4 eV) [50,69,70]. Oxygenated nitrogen was detected by XPS appears in the N K-edge spectrum as a weak shoulder at 404.0 eV. The main difference between the spectra of NC and mNC is an extra peak at 400.0 eV, with shoulders on the higher-energy side around 400.4 eV (all features are denoted as N_a). This peak coincides with the N_h peak in the spectrum of NC, but it is doubtful that the treatment of pre-activated NC with ammonia will only lead to the incorporation of hydrogenated nitrogen into aromatic rings. According to the XPS N 1s spectrum of mNC, the most probable scenario is the formation of predominantly imine, amine and amide groups at the edges of carbon defects. According to reported NEXAFS data, N $1s \rightarrow \pi^*$ excitations in unsaturated imine ($C=N-$) and amine ($-NH_2$) groups give a resonance at ~ 399.0 – 400.8 eV, while transitions in amide ($-C(O)NH_2$) groups appear at higher energies of 401.0 – 401.4 eV [56,67,71]. It should be noted that the peaks N_p and N_g become weaker and wider in the mNC spectrum due to the lower concentration of the pyridinic and graphitic nitrogen states in the modified sample.

2.2. Electrochemical Performance

To study the effect of the two-stage modification of NC on its ability to accumulate Na, galvanostatic and cyclic voltammetry (CV) tests were carried out. The electrical resistivity measured in the four-point configuration is 0.095 ± 0.019 Ohm m for mNC, which is slightly lower than 0.130 ± 0.026 Ohm m for NC. Figure 4a presents the discharge–charge capacity and Coulombic efficiency of NC and mNC electrodes at current densities of 0.05, 0.1, 0.25, 0.5, 1.0, and 0.05 A g^{-1} each for 10 cycles. Both electrodes exhibit a high initial irreversible capacity due to the formation of solid–electrolyte interphase (SEI) layers on their large surface areas. The values of the initial discharge capacity and its drop are greater for mNC since the electrode has a more developed surface area. Upon reaching the tenth cycle at 0.05 A g^{-1} , the reversible discharge capacity is 152 mA h g^{-1} for NC and 279 mA h g^{-1} for mNC. The specific capacity is 99 mA h g^{-1} for NC and 160 mA h g^{-1} for mNC at 1.0 A g^{-1} , since sodium ion diffusion is slower at high current densities. The subsequent decrease in the current density to 0.05 A g^{-1} provides the capacity values of 135 and 253 mA h g^{-1} for NC and mNC, respectively.

The galvanostatic profiles for NC and mNC at the 60th cycle exhibit only a sloping region, associated with sodium adsorption on the electrode surface, and have a nonessential plateau region at a voltage less than 0.1 V which originated from the sodium insertion into the graphite interlayer space (Figure 4b) [3]. The modified mNC shows a higher slopping capacity than the initial NC due to the presence of new oxygen- and nitrogen-containing functional groups and a higher plateau capacity caused by the availability of an interlayer space as a result of the etching of carbon shells. The CV curves measured for NC and mNC at a scan rate of 0.1 mV s^{-1} have a pair of narrow redox peaks around 0.1 V due to sodium intercalation (Figure 4c,d). Similar to the results obtained from the analysis of the discharge–charge curves, the CV curve of the mNC electrode has a shape closer to a rectangle in the high voltage region and more pronounced redox peaks at 0.1 V than that of the NC electrode. Thus, a 50% increased capacity of the modified sample is provided both in the region of high and low voltage due to increased adsorption of sodium ions on the modified surface and improved intercalation between graphitic-like layers.

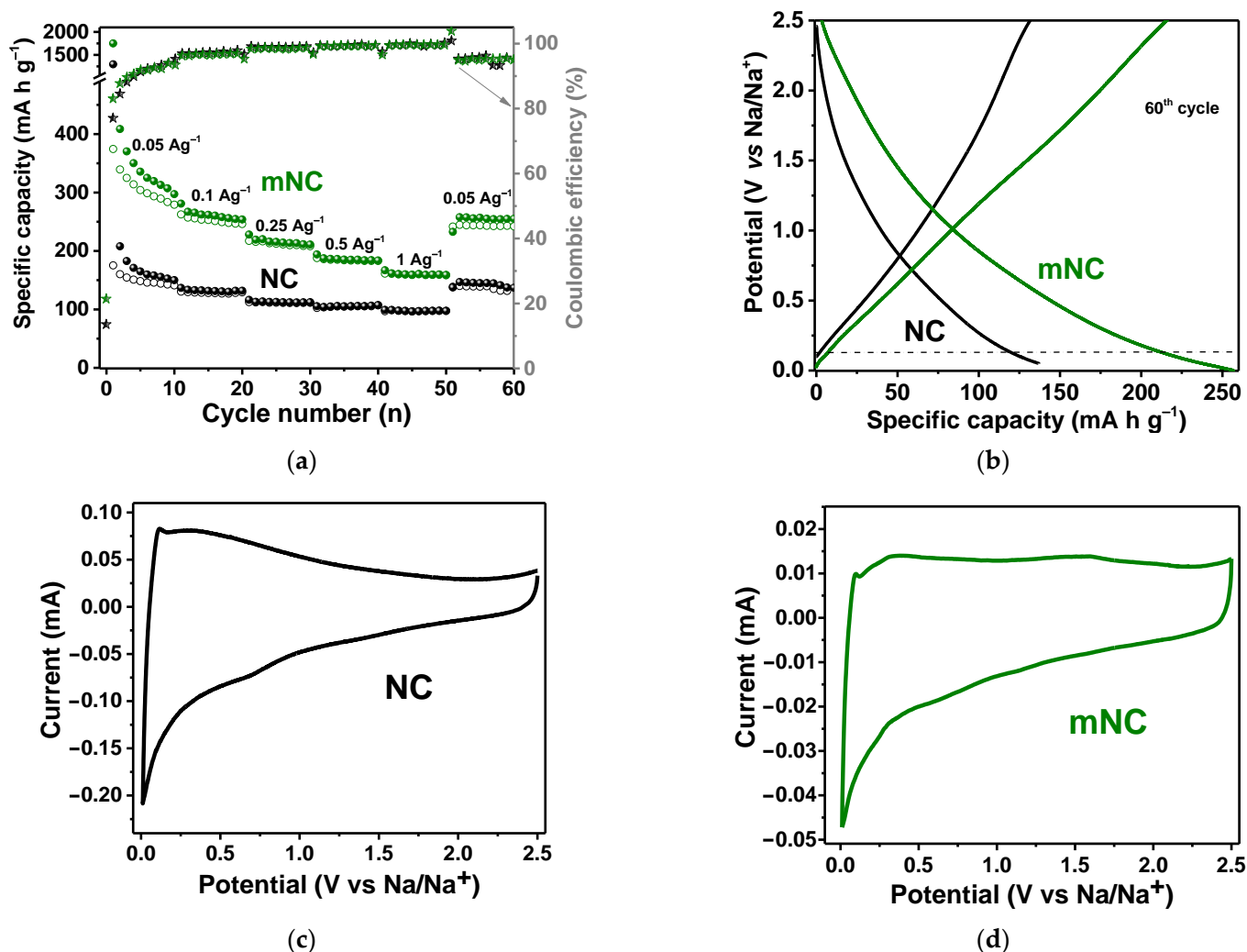


Figure 4. Electrochemical performance of NC and mNC in sodium-ion batteries: (a) rate capability at current densities of 0.05–1.00 A g⁻¹; (b) discharge–charge curves at 60th cycles at 0.05 A g⁻¹; CV curves measured at 0.1 mV s⁻¹ for (c) NC and (d) mNC.

The NC and mNC were tested as working electrodes of SCs in three-electrode cells using 1 M H₂SO₄ and 6 M KOH electrolytes. The electrode surface is sensitive to contact with an electrolyte and changes due to electroadsorption of ions or ionization of covalently bound functional groups. CV curves were recorded in a 1 V potential window (from 0 to 1 V for 1 M H₂SO₄ and from -1 to 0 V for 6 M KOH) at scan rates of 2–200 mV s⁻¹. Figure 5a,b show CV curves at a slow scan rate of 5 mV s⁻¹. For NC, the quasi-rectangular shape of the CV curves for both electrolytes without any redox peaks indicates a double-layer capacitive behavior of the NC electrode. The CV loop of mNC has a larger area than that of NC and shows a set of redox peaks around 0.2/0.7 V for 1 M H₂SO₄ and at -0.4/-0.9 V for 6 M KOH, indicating pseudo-capacitive contributions to electrochemical charge storage. In acidic media, these peaks can be attributed to the reversible protonation of pyridinic N and imine groups, while in alkaline media, hydroxyl and amine groups can easily interact with negatively charged hydroxyl ions. Dependencies of the gravimetric capacitance of NC and mNC on the potential scan rate are presented in Figure 5c,d. In an acidic electrolyte, the initial NC sample exhibits the specific capacitance of 125 F g⁻¹ at a scan rate of 2 mV s⁻¹, and 18 F g⁻¹ at 200 mV s⁻¹. The modified mNC sample shows the larger values of 172 at 2 mV s⁻¹ and 37 F g⁻¹ at 200 mV s⁻¹. In alkaline electrolyte, the specific capacitance of NC is 123 at 2 mV s⁻¹ and 8 F g⁻¹ at 200 mV s⁻¹, and, after the

modification process, it increases to 151 F g^{-1} at 2 mV s^{-1} and 10 F g^{-1} at 200 mV s^{-1} . Thus, it turns out that a large surface area of micropores, formed as a result of NC modification, becomes available for ion adsorption and increases the electrical double-layer capacitance. Moreover, the presence of new nitrogen and oxygen surface groups in mNC leads to a pseudocapacitance contribution.

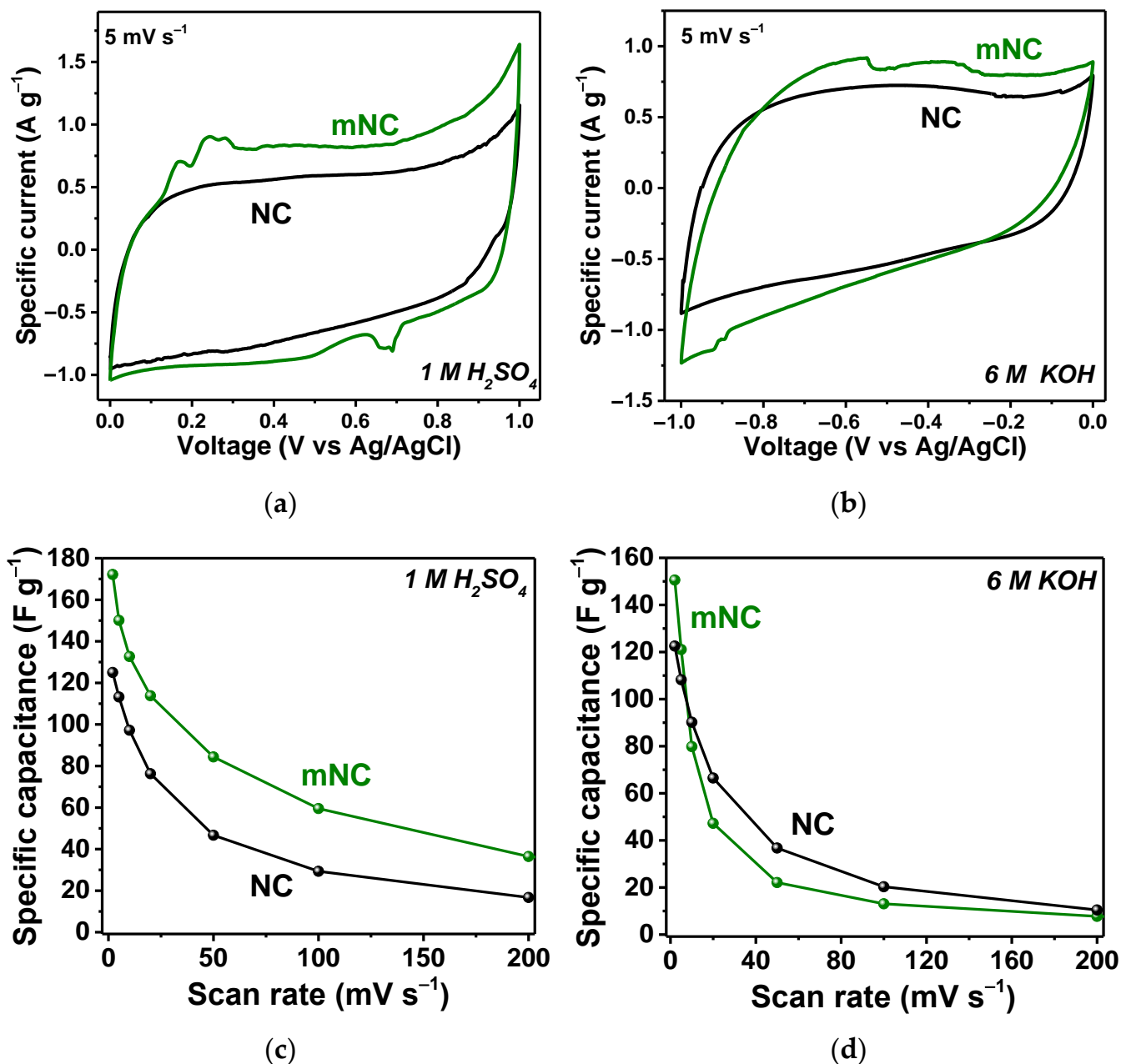


Figure 5. Electrochemical performances of NC and mNC electrodes in aqueous SCs: CV curves at 5 mV s^{-1} in (a) $1 \text{ M H}_2\text{SO}_4$ and (b) 1 M KOH electrolytes; Gravimetric capacitance at scan rates of $2\text{--}200 \text{ mV s}^{-1}$ in (c) $1 \text{ M H}_2\text{SO}_4$ and (d) 1 M KOH electrolytes.

According to the data from the literature, microporous carbons with sub-nanometer pores demonstrated a better ability to accumulate charge in aqueous SCs than mesoporous carbons [72,73]. At the same time, the importance of the presence of mesopores, through which electrolyte ions reach micropores, is also noted. NC materials enriched with micropores with a large surface area of $1000\text{--}3000 \text{ m}^2 \text{ g}^{-1}$ can have a capacitance in the range of $300\text{--}700 \text{ F g}^{-1}$ at low current densities of $0.5\text{--}0.5 \text{ A g}^{-1}$. In our case, the NC sample is

enriched with mesopores of 2–27 nm in size and has a very small contribution of micropores even after its two-stage modification (micropore volume less than $0.2 \text{ cm}^3 \text{ g}^{-1}$). For this reason, the best capacitance values are 172 F g^{-1} in $1 \text{ M H}_2\text{SO}_4$ and 151 F g^{-1} in 6 M KOH for mNC. They are in good agreement with previously reported data for various nitrogen-doped carbon materials (Table S1).

The long-term electrochemical cycling stability of mNC electrode was evaluated in a SIB half-cell and a symmetric SC with $1 \text{ M H}_2\text{SO}_4$ electrolyte. Figure 6a shows the change in the specific capacity of SIB at current densities 0.05 , 0.25 , and 0.50 A g^{-1} for 270 cycles. The capacity loss is $\sim 10\%$ at both 0.25 and 0.50 A g^{-1} for every hundred cycles at a given current density. In the symmetric SC, the initial specific capacitance of 76 F g^{-1} decreased to 53 F g^{-1} after 10,000 cycles at a scan rate of 200 mV s^{-1} (Figure 6b). Consequently, the capacitance retention of the mNC electrode under these conditions is 70%.

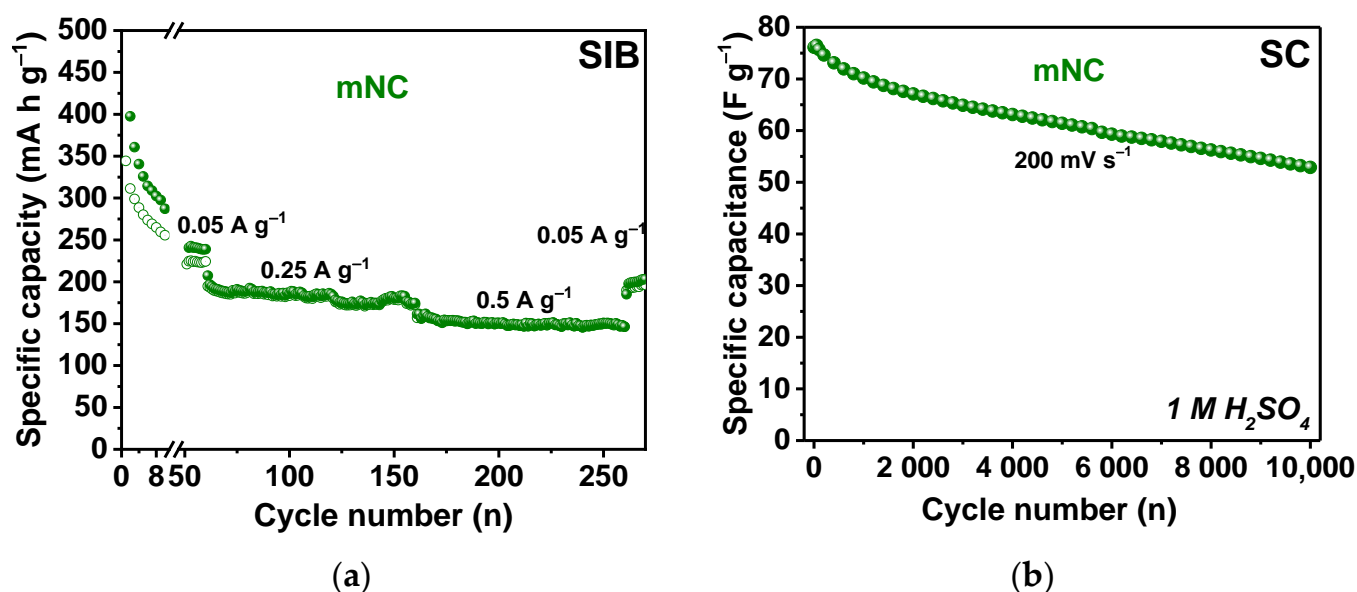


Figure 6. Long-term stability measurements of the mNC electrode in (a) half-cell SIB at current densities of 0.05 , 0.25 and 0.5 A g^{-1} for total 270 cycles and (b) symmetric SC with $1 \text{ M H}_2\text{SO}_4$ electrolyte at a scan rate of 200 mV s^{-1} for 10,000 cycles.

3. Discussion

Electrochemical experiments reveal an improvement in the performance of NC after the two-stage chemical modification procedure in SIBs and SCs with both acidic and alkaline electrolytes. It should be noted that tests of the NC electrode after the first stage of modification, which consisted in chemical activation with a KOH melt, showed no improvement of the electrochemical properties in SIBs and SCs with an acidic electrolyte (Figure S3a,b). This can be explained by the fact that a small amount of micropores with hydroxyl-terminated edges in the KOH-activated NC does not improve ion permeability [43]. Although only for SC with an alkaline electrolyte, the specific capacitance of this electrode increases by $8\text{--}16 \text{ F g}^{-1}$ (Figure S3c). Hydroxyl ions from an alkaline aqueous solution react with $-\text{OH}$ and $-\text{NH}_2$ groups, formed at the edges of vacancies as a result of treatment of the NC material with KOH [74–77]. In addition, oxygen- and nitrogen-containing groups can sterically close the pores and prevent the penetration of sodium ions and protons into the internal volume of the activated sample. The second stage of the modification used, which consists of hydrothermal treatment with ammonia, affects the chemical state of the surface of pre-activated NC and, apparently, is the main reason for the significant improvement of its electrochemical performance in SIBs and SCs. Our previous study revealed that hydrothermal treatment of as-prepared porous NC material in ammonia solution under the same conditions leads to the incorporation of edge pyri-

dinic N, hydrogenated N, and carbonyl groups and the formation of micropores 1.4 nm in size [43]. Testing of this NC in SIBs and SCs revealed an improvement in its electrochemical performance after modification.

In this work, it is shown that oxygen functionalities formed on the NC surface as a result of KOH treatment react with ammonia under hydrothermal conditions. FTIR, XPS, and NEXAFS spectroscopies revealed that, in addition to pyridinic N and hydrogenated pyridinic N, various types of hydrogenated nitrogen are formed such as amine, imine, and amide groups. These nitrogen-containing groups play a key role in the electrochemical properties of mNC and, according to CV data of mNC electrodes in SIBs and SCs (Figures 4c,d and 5a,b), they are actively involved in redox reactions. To explain the outstanding electrochemical properties of NC electrodes, the identification of the particular type of nitrogen state responsible for storing Na^+ ions and reacting with H^+ and OH^- ions is still under discussion. Numerous studies confirm that pyridinic N is responsible for the accumulation of alkali metal ions [78], as well as for redox reactions with protons in aqueous SCs [79]. However, there are articles that report the interaction of alkali metals with hydrogenated N and with carbon near graphitic N configurations [70,80]. The quantum-chemical calculations have shown that the binding energy of Na with amide N (-2.5 eV) is higher than that with pyridinic N (-2.3 eV) [31].

In Figure 7, we summarize the nitrogen- and oxygen-containing groups, which are formed as a result of the two-stage modification of NC and can participate in reversible redox reactions. For SIBs, the increased capacity of mNC can be explained mainly by the adsorption of Na^+ ions on pyridinic, hydrogenated pyridinic and amide N states (Figure 7a). In the case of SCs with an acidic electrolyte, protons react with pyridinic and imine N to form hydrogenated pyridinic and amine N [59,61] (Figure 7b). Hydroxyl and amine groups found in mNC can react with hydroxyl ions of an alkaline electrolyte, leading to the formation of carbonyl and imine groups [61] (Figure 7c). As a result of the applied modification procedure, a set of nitrogen- and oxygen-containing groups is formed at the edge of defects, leading to an improvement in the performance of SIBs and SCs with acidic and alkaline electrolytes.

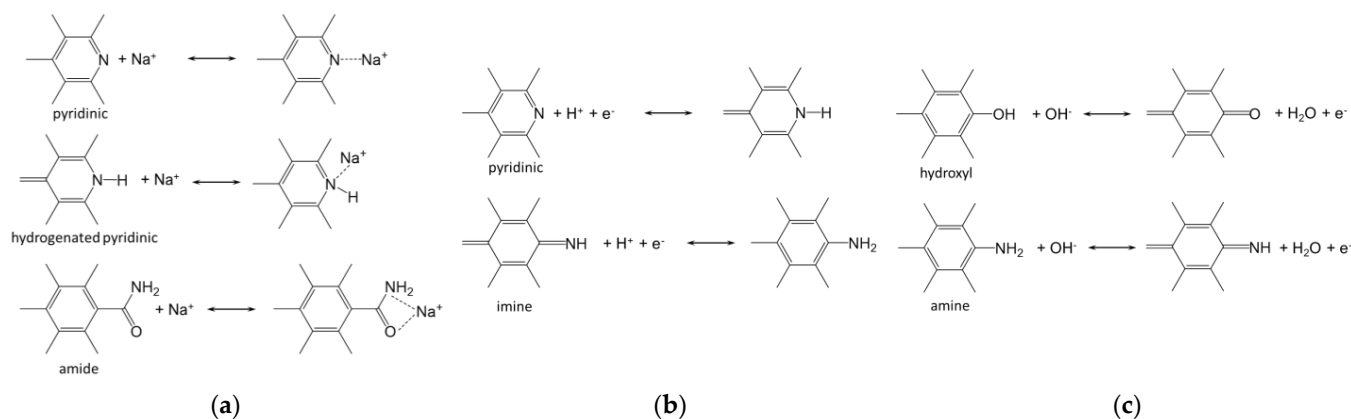


Figure 7. Assumed reversible redox reactions involving functional groups of NC in (a) SIBs and SCs in (b) acidic electrolyte and (c) alkaline electrolyte.

In addition, hydrothermal activation can lead to the additional etching of carbon shells and to the formation of more micropores and small mesopores. The adsorbed ions begin to penetrate into the interior of the carbon shells and then adsorb onto the pore walls. According to DFT calculations, sodium adsorbed in a multi-walled carbon nanotube between a partially unzipped outer carbon shell and an intact inner carbon shell has a binding energy 0.3 eV higher than that of an undamaged nanotube [81]. Thus, the more open structure of the mNC electrode helps to minimize the diffusion path of electrolyte ions, which is crucial for charging electrochemical devices. The trend to increase the electrostatic double-layer capacitance at higher scan rates and Na^+ ion storage capacity at high current

densities for mNC can be attributed to the faster electrochemical kinetics of electrostatic adsorption of ions, especially on the more accessible inner surface of the modified sample than that for initial NC.

4. Materials and Methods

4.1. Synthesis

The NC sample was synthesized using acetonitrile as a source of carbon and nitrogen and as a template for CaO nanoparticles obtained by pyrolysis of calcium tartrate at a temperature of 750 °C for 10 min under an argon atmosphere. Details of the synthesis of NC are described in [50,82]. Acetonitrile vapors were introduced in a CVD reactor heated at 750 °C for 30 min in order to grow NC on the surface of template CaO nanoparticles. After that, CaO was removed from the product with diluted hydrochloric acid. A mixture of NC and KOH (3:1 by weight) was heated in argon at 750 °C for 2 h. To remove KOH, the sample was washed with distilled water. The second stage of modification is the hydrothermal activation of KOH-treated sample in an aqueous solution of ammonia (9 wt.%) using the procedure described in [43]. In brief, 50 mg of NC activated by KOH and 8 mL of the ammonia solution were put in a Teflon reactor. The reactor was placed inside a hermetically sealed autoclave and then heated to a temperature of 147 °C for 30 h. After cooling, the synthesis product was dried in an oven at 80 °C for 12 h. The sample after two stages of modification was denoted as mNC.

4.2. Characterization

Raman scattering was measured using a LabRAM HR Evolution (Horiba, Kyoto, Japan) spectrometer. The spectra were excited with the focused beam of an Ar⁺ laser operating at a wavelength of 514 nm. Transmission FTIR spectra were recorded on an FTS 2000 Scimitar spectrometer (Digilab, Holliston, MA, USA) in a mid-infrared region from 400 to 4000 cm⁻¹. To obtain a transparent pellet as a probe for FTIR, the samples were mixed with potassium bromide. Nitrogen adsorption experiments were carried out on a Quantochrome's Autosorb iQ analyzer (Quantochrome Instruments, Boynton Beach, FL, USA) at a temperature of 77 K. The samples were first evacuated under a dynamic vacuum at 200 °C for 6 h. The adsorption–desorption isotherms of N₂ were measured within the range of relative pressures P/P_0 of 10⁻⁶ to 0.995. The specific surface area was calculated from the data obtained based on the conventional Brunauer–Emmett–Teller model. Pore volume and pore size distributions were calculated using the DFT approach. The fitting error was less than 0.5%.

XPS and NEXAFS spectroscopy experiments were performed at the Russian–German Beamline (RGLB) at the BESSY II synchrotron radiation facility, Helmholtz-Zentrum Berlin für Materialien und Energie (HZB, Berlin, Germany). The powder samples were deposited on copper substrates, which were placed on a holder in a vacuum chamber (10⁻⁹ Torr). The photon energy of 830 eV was used in XPS measurements. The binding energy scale was calibrated to the position of the Au 4f_{7/2} line at 84 eV for a clean Au foil. The core-level spectra were fitted using a Gaussian/Lorentzian product function and a Shirley-type background within Casa XPS software, Version 2.3.15 (Casa Software Ltd., Teignmouth, UK). The NEXAFS spectra were recorded in the leakage current measurement mode.

The electrical resistance of NC and mNC was measured according to the procedure described in [83]. Samples were pressed into quartz cylindrical capillaries and four-probe measurements were performed at a current of 2 mA.

4.3. Preparation of Electrodes and Electrochemical Tests

A mixture of the carbon sample, a conductive additive (carbon black, super-P) and binder (polyvinylidene fluoride, PVDF) was prepared using N-methyl-2-pyrrolidone (NMP) solvent. The ratio of the components was 8:1:1 by weight. A piece of a copper foil was uniformly covered with a thin layer of the resulting paste-like mixture and dried in a vacuum oven at 80 °C for 12 h. Coin-type CR2032 cells were assembled in an argon-filled glovebox

using carbon on copper as a working electrode, sodium metal as a counter electrode, glass fiber as a separator, and 1 M NaClO₄ in ethylene carbonate-dimethyl carbonate as electrolyte. A galvanostatic study of SIBs was carried out on a NEWARE CT-3008 test station (Neware Technology Ltd., Shenzhen, China) in the voltage range from 0.01 to 2.50 V relative to Na/Na⁺ and current densities from 0.05 to 1 A g⁻¹. After 60 cycles, the cells were used for the CV measurements on a BCS-805 system at a scan rate of 0.1 mV s⁻¹.

Working electrodes for SCs were prepared by mixing a carbon sample with an aqueous suspension of Teflon F-4D and ethanol, followed by homogenization through repeated rolling into a film. The film was applied on a Pt current collector. This electrode and the Pt counter electrode were separated by a 20 μm-thick polypropylene cloth impregnated with 1 M H₂SO₄ or 6 M KOH electrolyte. An Ag/AgCl electrode filled with a saturated KCl aqueous solution was used as a reference electrode in three-electrode cells. CV curves were recorded on a SP-300 potentiostat/galvanostat (Biologic, Seyssinet-Pariset, France) at scan rates 2–200 mV s⁻¹. A voltage range was from 0 to +1 V vs. Ag/AgCl for the cells with 1 M H₂SO₄ electrolyte and from –1 to 0 V vs. Ag/AgCl for the cells with 6 M KOH electrolyte. The specific capacitance was calculated from the area of CV curves as: $C = \frac{\oint i du}{2 \cdot \Delta U \cdot V_s \cdot m}$, where *i* is the current (A), *du* is the potential change (V), Δ*U* is the voltage window (V), *V*_s is the scan rate (V s⁻¹), and *m* is the weight of carbon material (g).

5. Conclusions

The thermal decomposition of acetonitrile on the pyrolysis product of calcium tartrate yielded a mesoporous graphitic-like material of the composition CN_{0.07}O_{0.04}, with a specific surface area of 440 m² g⁻¹ and a pore volume of 1.4 cm³ g⁻¹. The two-stage chemical modification of this material, performed by heating with potassium hydroxide at 750 °C for 2 h followed by hydrothermal treatment in ammonia at 147 °C for 30 h made it possible to increase the specific surface area up to 1180 m² g⁻¹ and the pore volume up to 1.8 cm³ g⁻¹ due to the etching of carbon shells and the formation of new pores in the range of 0.6–1.5 nm. The modified sample contained 4% nitrogen, mainly in the form of pyridinic N, hydrogenated pyridinic N, imine, amine, and amide groups. Electrochemical tests of carbon electrodes in SIB cells at current densities of 0.05–1.00 A g⁻¹ revealed a gravimetric capacity in the range of 135–99 mA h g⁻¹ for the initial sample, as well as an increased capacity of 253–160 mA h g⁻¹ and a long cycling performance for the chemically modified sample. The two-stage modified sample also showed an improved performance in SCs. At a scan rate of 2 mV s⁻¹, the specific capacitance was 172 F g⁻¹ in the 1 M H₂SO₄ electrolyte and 151 F g⁻¹ in the 6 M KOH electrolyte. The outstanding energy storage performance of N-doped carbon after the modification with KOH and aqueous ammonia solution is explained by (1) extra-active surface sites for the adsorption of ions due to the creation and opening of nanopores, (2) better diffusion of ions through a 3D carbon matrix by increasing the number of mesopores, and (3) the decisive role of imine, amine, and amide groups in reversible electrochemical reactions with ions.

Supplementary Materials: The following supporting information can be downloaded at: <https://www.mdpi.com/article/10.3390/inorganics10110198/s1>, Figure S1: Nitrogen adsorption–desorption isotherms at 77 K and DFT pore size distributions of NC and NC after the treatment with potassium hydroxide; Figure S2: XPS survey, C 1s, N 1s and O 1s spectra of NC after the treatment with potassium hydroxide; Figure S3: Rate capability of NC and NC after KOH-treatment electrodes at current densities of 0.05–1.00 A g⁻¹ in SIBs cell; Gravimetric capacitance of NC and NC after KOH-treatment at scan rates of 2–200 mV s⁻¹ in 1 M H₂SO₄ and 1 M KOH electrolytes in supercapacitors; Table S1: Capacitance in aqueous supercapacitors in 1 M H₂SO₄ and 6 M KOH electrolytes and capacity in sodium-ion batteries for nitrogen-doped carbon materials, reported in the literature [84–105].

Author Contributions: Conceptualization, Y.V.F.; methodology, A.A.M.; validation, L.G.B. and A.V.O.; investigation, Y.V.F., S.G.S., A.A.V., E.V.S., A.D.N., M.A.G., K.A.K. and A.A.M.; writing—original draft preparation, Y.V.F.; writing—review and editing, A.D.N., S.G.S., E.V.S., A.V.O. and L.G.B.; project administration, Y.V.F. All authors have read and agreed to the published version of the manuscript.

Funding: This research was funded by the Russian Science Foundation (grant 19-73-10068). The measurements of FTIR spectra were supported by the Ministry of Science and Higher Education of the Russian Federation (project 121031700314-5). A.A.M. acknowledges BMBF (grant no. 05K19KER).

Institutional Review Board Statement: Not applicable.

Informed Consent Statement: Not applicable.

Data Availability Statement: Not applicable.

Acknowledgments: The authors thank the Helmholtz-Zentrum Berlin für Materialien und Energie for the allocation of beamtime for XPS and NEXAFS measurements and support within the Russian German Laboratory at BESSY II.

Conflicts of Interest: The authors declare no conflict of interest.

References

1. Zhang, T.; Li, C.; Wang, F.; Noori, A.; Mousavi, M.F.; Xia, X.; Zhang, Y. Recent Advances in Carbon Anodes for Sodium-Ion Batteries. *Chem. Rec.* **2022**, *22*, e202200083. [[CrossRef](#)] [[PubMed](#)]
2. Lenchuk, O.; Adelhelm, P.; Mollenhauer, D. New Insights into the Origin of Unstable Sodium Graphite Intercalation Compounds. *Phys. Chem. Chem. Phys.* **2019**, *21*, 19378–19390. [[CrossRef](#)] [[PubMed](#)]
3. Yuan, M.; Cao, B.; Liu, H.; Meng, C.; Wu, J.; Zhang, S.; Li, A.; Chen, X.; Song, H. Sodium Storage Mechanism of Nongraphitic Carbons: A General Model and the Function of Accessible Closed Pores. *Chem. Mater.* **2022**, *34*, 3489–3500. [[CrossRef](#)]
4. Stolyarova, S.G.; Fedoseeva, Y.V.; Baskakova, K.I.; Vorfolomeeva, A.A.; Shubin, Y.V.; Makarova, A.A.; Bulusheva, L.G.; Okotrub, A.V. Bromination of Carbon Nanohorns to Improve Sodium-Ion Storage Performance. *Appl. Surf. Sci.* **2022**, *580*, 152238. [[CrossRef](#)]
5. Fedosova, A.A.; Stolyarova, S.G.; Shubin, Y.V.; Makarova, A.A.; Gusel'nikov, A.V.; Okotrub, A.V.; Bulusheva, L.G. Sodium Storage Properties of Thin Phosphorus-Doped Graphene Layers Developed on the Surface of Nanodiamonds under Hot Pressing Conditions. *Fuller. Nanotub. Carbon Nanostructures* **2020**, *28*, 335–341. [[CrossRef](#)]
6. Dou, X.; Hasa, I.; Saurel, D.; Vaalma, C.; Wu, L.; Buchholz, D.; Bresser, D.; Komaba, S.; Passerini, S. Hard Carbons for Sodium-Ion Batteries: Structure, Analysis, Sustainability, and Electrochemistry. *Mater. Today* **2019**, *23*, 87–104. [[CrossRef](#)]
7. Alvira, D.; Antorán, D.; Manyà, J.J. Plant-Derived Hard Carbon as Anode for Sodium-Ion Batteries: A Comprehensive Review to Guide Interdisciplinary Research. *Chem. Eng. J.* **2022**, *447*, 137468. [[CrossRef](#)]
8. Saurel, D.; Orayech, B.; Xiao, B.; Carriazo, D.; Li, X.; Rojo, T. From Charge Storage Mechanism to Performance: A Roadmap toward High Specific Energy Sodium-Ion Batteries through Carbon Anode Optimization. *Adv. Energy Mater.* **2018**, *8*, 1703268. [[CrossRef](#)]
9. Sarkar, S.; Roy, S.; Hou, Y.; Sun, S.; Zhang, J.; Zhao, Y. Recent Progress in Amorphous Carbon-Based Materials for Anodes of Sodium-Ion Batteries. *ChemSusChem* **2021**, *14*, 3693–3723. [[CrossRef](#)]
10. Liu, T.; Li, X. Biomass-Derived Nanostructured Porous Carbons for Sodium Ion Batteries: A Review. *Mater. Technol.* **2019**, *34*, 232–245. [[CrossRef](#)]
11. Yuan, Y.; Chen, Z.; Yu, H.; Zhang, X.; Liu, T.; Xia, M.; Zheng, R.; Shui, M.; Shu, J. Heteroatom-Doped Carbon-Based Materials for Lithium and Sodium Ion Batteries. *Energy Storage Mater.* **2020**, *32*, 65–90. [[CrossRef](#)]
12. Lee, J.; Kim, J.; Hyeon, T. Recent Progress in the Synthesis of Porous Carbon Materials. *Adv. Mater.* **2006**, *18*, 2073–2094. [[CrossRef](#)]
13. Jiang, G.; Senthil, R.A.; Sun, Y.; Kumar, T.R.; Pan, J. Recent Progress on Porous Carbon and Its Derivatives from Plants as Advanced Electrode Materials for Supercapacitors. *J. Power Sources* **2022**, *520*, 230886. [[CrossRef](#)]
14. Wahid, M.; Puthusseri, D.; Gawli, Y.; Sharma, N.; Ogale, S. Hard Carbons for Sodium-Ion Battery Anodes: Synthetic Strategies, Material Properties, and Storage Mechanisms. *ChemSusChem* **2018**, *11*, 506–526. [[CrossRef](#)]
15. Li, Y.; Pu, Z.; Sun, Q.; Pan, N. A Review on Novel Activation Strategy on Carbonaceous Materials with Special Morphology/Texture for Electrochemical Storage. *J. Energy Chem.* **2021**, *60*, 572–590. [[CrossRef](#)]
16. Wiggins-Camacho, J.D.; Stevenson, K.J. Effect of Nitrogen Concentration on Capacitance, Density of States, Electronic Conductivity, and Morphology of N-Doped Carbon Nanotube Electrodes. *J. Phys. Chem. C* **2009**, *113*, 19082–19090. [[CrossRef](#)]
17. Agrawal, A.; Janakiraman, S.; Biswas, K.; Venimadhav, A.; Srivastava, S.K.; Ghosh, S. Understanding the Improved Electrochemical Performance of Nitrogen-Doped Hard Carbons as an Anode for Sodium Ion Battery. *Electrochim. Acta* **2019**, *317*, 164–172. [[CrossRef](#)]

18. Shen, W.; Wang, C.; Xu, Q.; Liu, H.; Wang, Y. Nitrogen-Doping-Induced Defects of a Carbon Coating Layer Facilitate Na-Storage in Electrode Materials. *Adv. Energy Mater.* **2015**, *5*, 1400982. [[CrossRef](#)]
19. Sedelnikova, O.V.; Fedoseeva, Y.V.; Romanenko, A.I.; Gusel'nikov, A.V.; Vilkov, O.Y.; Maksimovskiy, E.A.; Bychanok, D.S.; Kuzhir, P.P.; Bulusheva, L.G.; Okotrub, A.V. Effect of Boron and Nitrogen Additives on Structure and Transport Properties of Arc-Produced Carbon. *Carbon* **2019**, *143*, 660–668. [[CrossRef](#)]
20. Bulusheva, L.G.; Okotrub, A.V.; Fedoseeva, Y.V.; Kurenaya, A.G.; Asanov, I.P.; Vilkov, O.Y.; Koós, A.A.; Grobert, N. Controlling Pyridinic, Pyrrolic, Graphitic, and Molecular Nitrogen in Multi-Wall Carbon Nanotubes Using Precursors with Different N/C Ratios in Aerosol Assisted Chemical Vapor Deposition. *Phys. Chem. Chem. Phys.* **2015**, *17*, 23741–23747. [[CrossRef](#)]
21. Scardamaglia, M.; Struzzi, C.; Aparicio Rebollo, F.J.; De Marco, P.; Mudimela, P.R.; Colomer, J.F.; Amati, M.; Gregoratti, L.; Petaccia, L.; Snyders, R.; et al. Tuning Electronic Properties of Carbon Nanotubes by Nitrogen Grafting: Chemistry and Chemical Stability. *Carbon* **2015**, *83*, 118–127. [[CrossRef](#)]
22. Vesel, A.; Zaplotnik, R.; Primc, G.; Mozetič, M. A Review of Strategies for the Synthesis of N-Doped Graphene-like Materials. *Nanomaterials* **2020**, *10*, 2286. [[CrossRef](#)] [[PubMed](#)]
23. Abbas, Q.; Raza, R.; Shabbir, I.; Olabi, A.G. Heteroatom Doped High Porosity Carbon Nanomaterials as Electrodes for Energy Storage in Electrochemical Capacitors: A Review. *J. Sci. Adv. Mater. Devices* **2019**, *4*, 341–352. [[CrossRef](#)]
24. Wu, J.; Pan, Z.; Zhang, Y.; Wang, B.; Peng, H. The Recent Progress of Nitrogen-Doped Carbon Nanomaterials for Electrochemical Batteries. *J. Mater. Chem. A* **2018**, *6*, 12932–12944. [[CrossRef](#)]
25. Lobiak, E.V.; Kuznetsova, V.R.; Makarova, A.A.; Okotrub, A.V.; Bulusheva, L.G. Structure, Functional Composition and Electrochemical Properties of Nitrogen-Doped Multi-Walled Carbon Nanotubes Synthesized Using Co–Mo, Ni–Mo and Fe–Mo Catalysts. *Mater. Chem. Phys.* **2020**, *255*, 123563. [[CrossRef](#)]
26. Guo, D.; Fu, Y.; Bu, F.; Liang, H.; Duan, L.; Zhao, Z.; Wang, C.; El-Toni, A.M.; Li, W.; Zhao, D. Monodisperse Ultrahigh Nitrogen-Containing Mesoporous Carbon Nanospheres from Melamine-Formaldehyde Resin. *Small Methods* **2021**, *5*, 2001137. [[CrossRef](#)]
27. Sun, J.; Sun, Y.; Oh, J.A.S.; Gu, Q.; Zheng, W.; Goh, M.; Zeng, K.; Cheng, Y.; Lu, L. Insight into the Structure-Capacity Relationship in Biomass Derived Carbon for High-Performance Sodium-Ion Batteries. *J. Energy Chem.* **2021**, *62*, 497–504. [[CrossRef](#)]
28. Zhang, Y.; Zhang, Z.; Tang, Y.; Jia, D.; Huang, Y.; Guo, Y.; Zhou, Z. Carbon Block Anodes with Columnar Nanopores Constructed from Amine-Functionalized Carbon Nanosheets for Sodium-Ion Batteries. *J. Mater. Chem. A* **2020**, *8*, 24393–24400. [[CrossRef](#)]
29. Sun, F.; Gao, J.; Yang, Y.; Zhu, Y.; Wang, L.; Pi, X.; Liu, X.; Qu, Z.; Wu, S.; Qin, Y. One-Step Ammonia Activation of Zhundong Coal Generating Nitrogen-Doped Microporous Carbon for Gas Adsorption and Energy Storage. *Carbon* **2016**, *109*, 747–754. [[CrossRef](#)]
30. Yang, C.; Qiao, C.; Chen, Y.; Zhao, X.; Wu, L.; Li, Y.; Jia, Y.; Wang, S.; Cui, X. Nitrogen Doped γ -Graphyne: A Novel Anode for High-Capacity Rechargeable Alkali-Ion Batteries. *Small* **2020**, *16*, 1907365. [[CrossRef](#)]
31. Gaddam, R.R.; Farokh Niaei, A.H.; Hankel, M.; Searles, D.J.; Kumar, N.A.; Zhao, X.S. Capacitance-Enhanced Sodium-Ion Storage in Nitrogen-Rich Hard Carbon. *J. Mater. Chem. A* **2017**, *5*, 22186–22192. [[CrossRef](#)]
32. Ou, J.; Yang, L.; Xi, X. Nitrogen-Rich Porous Carbon Anode with High Performance for Sodium Ion Batteries. *J. Porous Mater.* **2017**, *24*, 189–192. [[CrossRef](#)]
33. Xiang, J.; Lv, W.; Mu, C.; Zhao, J.; Wang, B. Activated Hard Carbon from Orange Peel for Lithium/Sodium Ion Battery Anode with Long Cycle Life. *J. Alloys Compd.* **2017**, *701*, 870–874. [[CrossRef](#)]
34. Sridhar, V.; Park, H. Sugar-Derived Disordered Carbon Nano-Sheets as High-Performance Electrodes in Sodium-Ion Batteries. *New J. Chem.* **2017**, *41*, 4286–4290. [[CrossRef](#)]
35. Farokh Niaei, A.H.; Roman, T.; Hussain, T.; Searles, D.J. Computational Study on the Adsorption of Sodium and Calcium on Edge-Functionalized Graphene Nanoribbons. *J. Phys. Chem. C* **2019**, *123*, 14895–14908. [[CrossRef](#)]
36. Zhou, M.; Pu, F.; Wang, Z.; Guan, S. Nitrogen-Doped Porous Carbons through KOH Activation with Superior Performance in Supercapacitors. *Carbon* **2014**, *68*, 185–194. [[CrossRef](#)]
37. Zhang, Z.; Xu, M.; Wang, H.; Li, Z. Enhancement of CO₂ Adsorption on High Surface Area Activated Carbon Modified by N₂, H₂ and Ammonia. *Chem. Eng. J.* **2010**, *160*, 571–577. [[CrossRef](#)]
38. Shaarani, F.W.; Hameed, B.H. Ammonia-Modified Activated Carbon for the Adsorption of 2,4-Dichlorophenol. *Chem. Eng. J.* **2011**, *169*, 180–185. [[CrossRef](#)]
39. Yang, H.; Lee, J.; Cheong, J.Y.; Wang, Y.; Duan, G.; Hou, H.; Jiang, S.; Kim, I.D. Molecular Engineering of Carbonyl Organic Electrodes for Rechargeable Metal-Ion Batteries: Fundamentals, Recent Advances, and Challenges. *Energy Environ. Sci.* **2021**, *14*, 4228–4267. [[CrossRef](#)]
40. Zhang, D.; Hao, Y.; Ma, Y.; Feng, H. Hydrothermal Synthesis of Highly Nitrogen-Doped Carbon Powder. *Appl. Surf. Sci.* **2012**, *258*, 2510–2514. [[CrossRef](#)]
41. Chen, H.; Song, Z.; Zhao, X.; Li, X.; Lin, H. Reduction of Free-Standing Graphene Oxide Papers by a Hydrothermal Process at the Solid/Gas Interface. *RSC Adv.* **2013**, *3*, 2971–2978. [[CrossRef](#)]
42. Liu, P.; Si, Z.; Lv, W.; Wu, X.; Ran, R.; Weng, D.; Kang, F. Synthesizing Multilayer Graphene from Amorphous Activated Carbon via Ammonia-Assisted Hydrothermal Method. *Carbon* **2019**, *152*, 24–32. [[CrossRef](#)]
43. Fedoseeva, Y.V.; Lobiak, E.V.; Shlyakhova, E.V.; Kovalenko, K.A.; Kuznetsova, V.R.; Vorfolomeeva, A.A.; Grebenkina, M.A.; Nishchakova, A.D.; Makarova, A.A.; Bulusheva, L.G.; et al. Hydrothermal Activation of Porous Nitrogen-Doped Carbon Materials for Electrochemical Capacitors and Sodium-Ion Batteries. *Nanomaterials* **2020**, *10*, 2163. [[CrossRef](#)] [[PubMed](#)]

44. Kopac, T.; Kirca, Y. Effect of Ammonia and Boron Modifications on the Surface and Hydrogen Sorption Characteristics of Activated Carbons from Coal. *Int. J. Hydrogen Energy* **2020**, *45*, 10494–10506. [[CrossRef](#)]
45. Wang, Y.; Zhang, L.; Hou, H.; Xu, W.; Duan, G.; He, S.; Liu, K.; Jiang, S. Recent Progress in Carbon-Based Materials for Supercapacitor Electrodes: A Review. *J. Mater. Sci.* **2021**, *56*, 173–200. [[CrossRef](#)]
46. Yang, L.; Guo, X.; Jin, Z.; Guo, W.; Duan, G.; Liu, X.; Li, Y. Emergence of Melanin-Inspired Supercapacitors. *Nano Today* **2021**, *37*, 101075. [[CrossRef](#)]
47. Cao, L.; Li, H.; Xu, Z.; Zhang, H.; Ding, L.; Wang, S.; Zhang, G.; Hou, H.; Xu, W.; Yang, F.; et al. Comparison of the Heteroatoms-Doped Biomass-Derived Carbon Prepared by One-Step Nitrogen-Containing Activator for High Performance Supercapacitor. *Diam. Relat. Mater.* **2021**, *114*, 108316. [[CrossRef](#)]
48. Cao, L.; Li, H.; Xu, Z.; Gao, R.; Wang, S.; Zhang, G.; Jiang, S.; Xu, W.; Hou, H. Camellia Pollen-Derived Carbon with Controllable N Content for High-Performance Supercapacitors by Ammonium Chloride Activation and Dual N-Doping. *ChemNanoMat* **2021**, *7*, 34–43. [[CrossRef](#)]
49. Han, X.; Xiao, G.; Wang, Y.; Chen, X.; Duan, G.; Wu, Y.; Gong, X.; Wang, H. Design and Fabrication of Conductive Polymer Hydrogels and Their Applications in Flexible Supercapacitors. *J. Mater. Chem. A* **2020**, *8*, 23059–23095. [[CrossRef](#)]
50. Shlyakhova, E.V.; Bulusheva, L.G.; Kanygin, M.A.; Plyusnin, P.E.; Kovalenko, K.A.; Senkovskiy, B.V.; Okotrub, A.V. Synthesis of Nitrogen-containing Porous Carbon Using Calcium Oxide. *Phys. Status Solidi* **2014**, *251*, 2607–2612. [[CrossRef](#)]
51. Ferrari, A.C.; Meyer, J.C.; Scardaci, V.; Casiraghi, C.; Lazzeri, M.; Mauri, F.; Piscanec, S.; Jiang, D.; Novoselov, K.S.; Roth, S.; et al. Raman Spectrum of Graphene and Graphene Layers. *Phys. Rev. Lett.* **2006**, *97*, 187401. [[CrossRef](#)]
52. Larkin, P. *Infrared and Raman Spectroscopy: Principles and Spectral Interpretation*; Elsevier: Stamford, CT, USA, 2017.
53. Bayu, A.; Nandiyanto, D.; Oktiani, R.; Ragadhita, R. How to Read and Interpret FTIR Spectroscopy of Organic Material. *Indones. J. Sci. Technol.* **2019**, *4*, 97–118. [[CrossRef](#)]
54. Ji, Y.; Yang, X.; Ji, Z.; Zhu, L.; Ma, N.; Chen, D.; Jia, X.; Tang, J.; Cao, Y. DFT-Calculated IR Spectrum Amide I, II, and III Band Contributions of N-Methylacetamide Fine Components. *ACS Omega* **2020**, *5*, 8572–8578. [[CrossRef](#)]
55. Dhopte, K.B.; Mohanapriya, K.; Jha, N.; Nemade, P.R. Enhanced Electrochemical Performance of Hyperbranched Poly(Amidographene). *Energy Storage Mater.* **2019**, *16*, 281–289. [[CrossRef](#)]
56. Khosravi, Z.; Kotula, S.; Lippitz, A.; Unger, W.E.S.; Klages, C.-P. IR- and NEXAFS-spectroscopic Characterization of Plasma-nitrogenated. *Plasma Process. Polym.* **2018**, *15*, 1700066. [[CrossRef](#)]
57. Ramanathan, T.; Fisher, F.T.; Ruoff, R.S.; Brinson, L.C. Amino-Functionalized Carbon Nanotubes for Binding to Polymers and Biological Systems. *Chem. Mater.* **2005**, *17*, 1290–1295. [[CrossRef](#)]
58. Scardamaglia, M.; Amati, M.; Llorente, B.; Mudimela, P.; Colomer, J.F.; Ghijsen, J.; Ewels, C.; Snyders, R.; Gregoratti, L.; Bittencourt, C. Nitrogen Ion Casting on Vertically Aligned Carbon Nanotubes: Tip and Sidewall Chemical Modification. *Carbon* **2014**, *77*, 319–328. [[CrossRef](#)]
59. Li, K.; Min, B.; Li, B. Preparation of Amide-Enriched Micro-Mesoporous Carbons from Bayberry Core via Prepolymerization and Ammonization Co-Treatment for High-Performance Supercapacitors. *Energy Rep.* **2022**, *8*, 648–660. [[CrossRef](#)]
60. Zhai, Y.; Pang, D.; Chen, H.; Xiang, B.; Chen, J.; Li, C.; Zeng, G.; Qiu, L. Effects of Ammonization on the Surface Physico-Chemical Properties of Sludge-Based Activated Carbon. *Appl. Surf. Sci.* **2013**, *280*, 590–597. [[CrossRef](#)]
61. Chen, C.M.; Zhang, Q.; Zhao, X.C.; Zhang, B.; Kong, Q.Q.; Yang, M.G.; Yang, Q.H.; Wang, M.Z.; Yang, Y.G.; Schlögl, R.; et al. Hierarchically Aminated Graphene Honeycombs for Electrochemical Capacitive Energy Storage. *J. Mater. Chem.* **2012**, *22*, 14076–14084. [[CrossRef](#)]
62. Jansen, R.J.J.; van Bekkum, H. XPS of Nitrogen-Containing Functional Groups on Activated Carbon. *Carbon* **1995**, *33*, 1021–1027. [[CrossRef](#)]
63. Kehrer, M.; Duchoslav, J.; Hinterreiter, A.; Cobet, M.; Mehic, A.; Stehrer, T.; Stifter, D. XPS Investigation on the Reactivity of Surface Imine Groups with TFAA. *Plasma Process. Polym.* **2019**, *16*, 1800160. [[CrossRef](#)]
64. Nowicki, P.; Pietrzak, R.; Wachowska, H. X-Ray Photoelectron Spectroscopy Study of Nitrogen-Enriched Active Carbons Obtained by Ammonoxidation and Chemical Activation of Brown and Bituminous Coals. *Energy Fuels* **2010**, *24*, 1197–1206. [[CrossRef](#)]
65. Bulusheva, L.G.; Stolyarova, S.G.; Chuvilin, A.L.; Shubin, Y.V.; Asanov, I.P.; Sorokin, A.M.; Mel'Gunov, M.S.; Zhang, S.; Dong, Y.; Chen, X.; et al. Creation of Nanosized Holes in Graphene Planes for Improvement of Rate Capability of Lithium-Ion Batteries. *Nanotechnology* **2018**, *29*, 134001. [[CrossRef](#)] [[PubMed](#)]
66. Fedoseeva, Y.V.; Pozdnyakov, G.A.; Okotrub, A.V.; Kanygin, M.A.; Nastaushev, Y.V.; Vilkov, O.Y.; Bulusheva, L.G. Effect of Substrate Temperature on the Structure of Amorphous Oxygenated Hydrocarbon Films Grown with a Pulsed Supersonic Methane Plasma Flow. *Appl. Surf. Sci.* **2016**, *385*, 464–471. [[CrossRef](#)]
67. Shard, A.G.; Whittle, J.D.; Beck, A.J.; Brookes, P.N.; Bullett, N.A.; Talib, R.A.; Mistry, A.; Barton, D.; McArthur, S.L. A NEXAFS Examination of Unsaturation in Plasma Polymers of Allylamine and Propylamine. *J. Phys. Chem. B* **2004**, *108*, 12472–12480. [[CrossRef](#)]
68. Sainio, S.; Wester, N.; Aarva, A.; Titus, C.J.; Nordlund, D.; Kauppinen, E.I.; Leppänen, E.; Palomäki, T.; Koehne, J.E.; Pitkänen, O.; et al. Trends in Carbon, Oxygen, and Nitrogen Core in the X-Ray Absorption Spectroscopy of Carbon Nanomaterials: A Guide for the Perplexed. *J. Phys. Chem. C* **2021**, *125*, 973–988. [[CrossRef](#)]

69. Leinweber, P.; Kruse, J.; Walley, F.L.; Gillespie, A.; Eckhardt, K.U.; Blyth, R.I.R.; Regier, T. Nitrogen K-Edge XANES—An Overview of Reference Compounds Used to Identify “unknown” Organic Nitrogen in Environmental Samples. *J. Synchrotron Radiat.* **2007**, *14*, 500–511. [\[CrossRef\]](#)
70. Lapteva, L.L.; Fedoseeva, Y.V.; Shlyakhova, E.V.; Makarova, A.A.; Bulusheva, L.G.; Okotrub, A.V. NEXAFS Spectroscopy Study of Lithium Interaction with Nitrogen Incorporated in Porous Graphitic Material. *J. Mater. Sci.* **2019**, *54*, 11168–11178. [\[CrossRef\]](#)
71. Graf, N.; Yegen, E.; Gross, T.; Lippitz, A.; Weigel, W.; Krakert, S.; Terfort, A.; Unger, W.E.S. XPS and NEXAFS Studies of Aliphatic and Aromatic Amine Species on Functionalized Surfaces. *Surf. Sci.* **2009**, *603*, 2849–2860. [\[CrossRef\]](#)
72. Ghosh, A.; Lee, Y.H. Carbon-Based Electrochemical Capacitors. *ChemSusChem* **2012**, *5*, 480–499. [\[CrossRef\]](#)
73. Liu, T.; Zhang, F.; Song, Y.; Li, Y. Revitalizing Carbon Supercapacitor Electrodes with Hierarchical Porous Structures. *J. Mater. Chem. A* **2017**, *5*, 17705–17733. [\[CrossRef\]](#)
74. Oh, Y.J.; Yoo, J.J.; Kim, Y.I.; Yoon, J.K.; Yoon, H.N.; Kim, J.H.; Park, S. Bin Oxygen Functional Groups and Electrochemical Capacitive Behavior of Incompletely Reduced Graphene Oxides as a Thin-Film Electrode of Supercapacitor. *Electrochim. Acta* **2014**, *116*, 118–128. [\[CrossRef\]](#)
75. Popov, K.M.; Fedoseeva, Y.V.; Kokhanovskaya, O.A.; Razd'yakonova, G.I.; Smirnov, D.A.; Bulusheva, L.G.; Okotrub, A.V. Functional Composition and Electrochemical Characteristics of Oxidized Nanosized Carbon. *J. Struct. Chem.* **2017**, *58*, 1187–1195. [\[CrossRef\]](#)
76. Fedoseeva, Y.V.; Shlyakhova, E.V.; Stolyarova, S.G.; Vorfolomeeva, A.A.; Grebenkina, M.A.; Makarova, A.A.; Shubin, Y.V.; Okotrub, A.V.; Bulusheva, L.G. Brominated Porous Nitrogen-Doped Carbon Materials for Sodium-Ion Storage. *Batteries* **2022**, *8*, 114. [\[CrossRef\]](#)
77. Jing, X.; Wang, L.; Qu, K.; Li, R.; Kang, W.; Li, H.; Xiong, S. KOH Chemical-Activated Porous Carbon Sponges for Monolithic Supercapacitor Electrodes. *ACS Appl. Energy Mater.* **2021**, *4*, 6768–6776. [\[CrossRef\]](#)
78. Samdani, J.S.; Tran, T.N.; Kang, T.H.; Lee, B.J.; Jang, Y.H.; Yu, J.S.; Shanmugam, S. The Identification of Specific N-Configuration Responsible for Li-Ion Storage in N-Doped Porous Carbon Nanofibers: An Ex-Situ Study. *J. Power Sources* **2021**, *483*, 229174. [\[CrossRef\]](#)
79. Jiang, B.; Tian, C.; Wang, L.; Sun, L.; Chen, C.; Nong, X.; Qiao, Y.; Fu, H. Highly Concentrated, Stable Nitrogen-Doped Graphene for Supercapacitors: Simultaneous Doping and Reduction. *Appl. Surf. Sci.* **2012**, *258*, 3438–3443. [\[CrossRef\]](#)
80. Bulusheva, L.G.; Kanygin, M.A.; Arkhipov, V.E.; Popov, K.M.; Fedoseeva, Y.V.; Smirnov, D.A.; Okotrub, A.V. In Situ X-Ray Photoelectron Spectroscopy Study of Lithium Interaction with Graphene and Nitrogen-Doped Graphene Films Produced by Chemical Vapor Deposition. *J. Phys. Chem. C* **2017**, *121*, 5108–5114. [\[CrossRef\]](#)
81. Saroja, A.P.V.K.; Muruganathan, M.; Muthusamy, K.; Mizuta, H.; Sundara, R. Enhanced Sodium Ion Storage in Interlayer Expanded Multiwall Carbon Nanotubes. *Nano Lett.* **2018**, *18*, 5688–5696. [\[CrossRef\]](#)
82. Nishchakova, A.D.; Grebenkina, M.A.; Shlyakhova, E.V.; Shubin, Y.V.; Kovalenko, K.A.; Asanov, I.P.; Fedoseeva, Y.V.; Makarova, A.A.; Okotrub, A.V.; Bulusheva, L.G. Porosity and Composition of Nitrogen-Doped Carbon Materials Templated by the Thermolysis Products of Calcium Tartrate and Their Performance in Electrochemical Capacitors. *J. Alloys Compd.* **2021**, *858*, 158259. [\[CrossRef\]](#)
83. Kuznetsov, V.L.; Butenko, Y.V.; Chuvilin, A.L.; Romanenko, A.I.; Okotrub, A.V. Electrical Resistivity of Graphitized Ultra-Disperse Diamond and Onion-like Carbon. *Chem. Phys. Lett.* **2001**, *336*, 397–404. [\[CrossRef\]](#)
84. Elmouwahidi, A.; Zapata-Benabithé, Z.; Carrasco-Marín, F.; Moreno-Castilla, C. Activated Carbons from Koh-Activation of Argan (*Argania Spinosa*) Seed Shells as Supercapacitor Electrodes. *Bioresour. Technol.* **2012**, *111*, 185–190. [\[CrossRef\]](#) [\[PubMed\]](#)
85. Kodama, M.; Yamashita, J.; Soneda, Y.; Hatori, H.; Nishimura, S.; Kamegawa, K. Structural Characterization and Electric Double Layer Capacitance of Template Carbons. *Mater. Sci. Eng. B* **2004**, *108*, 156–161. [\[CrossRef\]](#)
86. Wang, Q.; Xia, W.; Guo, W.; An, L.; Xia, D. Zou, R. Functional Zeolitic-Imidazolate-Framework-Templated Porous Carbon Materials for CO₂ Capture and Enhanced Capacitors. *Chem.-Asian J.* **2013**, *8*, 1879–1885. [\[CrossRef\]](#)
87. Lee, Y.-H.; Chang, K.-H.; Hu, C.-C. Differentiate the Pseudocapacitance and Double-Layer Capacitance Contributions for Nitrogen-Doped Reduced Graphene Oxide in Acidic and Alkaline Electrolytes. *J. Power Sources* **2013**, *227*, 300–308. [\[CrossRef\]](#)
88. Wang, Q.; Yan, J.; Fan, Z. Nitrogen-Doped Sandwich-like Porous Carbon Nanosheets for High Volumetric Performance Supercapacitors. *Electrochim. Acta* **2014**, *146*, 548–555. [\[CrossRef\]](#)
89. Zhang, W.; Ren, Z.; Ying, Z.; Liu, X.; Wan, H. Activated Nitrogen-Doped Porous Carbon Ensemble on Montmorillonite for High-Performance Supercapacitors. *J. Alloys Compd.* **2018**, *743*, 44–51. [\[CrossRef\]](#)
90. Ornelas, O.; Sieben, J.M.; Ruiz-Rosas, R.; Morallón, E.; Cazorla-Amorós, D.; Geng, J.; Soin, N.; Siores, E.; Johnson, B.F. On the Origin of the High Capacitance of Nitrogen-Containing Carbon Nanotubes in Acidic and Alkaline Electrolytes. *Chem. Commun.* **2014**, *50*, 11343–11346. [\[CrossRef\]](#)
91. Lv, L.-P.; Wu, Z.-S.; Chen, L.; Lu, H.; Zheng, Y.-R.; Weidner, T.; Feng, X.; Landfester, K.D. Crespy, Precursor-controlled and template-free synthesis of nitrogen-doped carbon nanoparticles for supercapacitors. *RSC Adv.* **2015**, *5*, 50063–50069. [\[CrossRef\]](#)
92. Liu, R.; Pan, L.; Wan, L.; Wu, D. An evaporation-induced tri-consistent assembly route towards nitrogen-doped carbon microfibers with ordered mesopores for high performance supercapacitors. *Phys. Chem. Chem. Phys.* **2015**, *17*, 4724–4729. [\[CrossRef\]](#)
93. Olejniczak, A.; Leżańska, M.; Pacuła, A.; Nowak, P.; Włoch, J.; Łukaszewicz, J.P. Nitrogen-containing mesoporous carbons with high capacitive properties derived from a gelatin biomolecule. *Carbon.* **2015**, *91*, 200–214. [\[CrossRef\]](#)

94. Zeng, R.; Tang, X.; Huang, B.; Yuan, K.; Chen, Y. Nitrogen-Doped Hierarchically Porous Carbon Materials with Enhanced Performance for Supercapacitor. *ChemElectroChem* **2018**, *5*, 515–522. [[CrossRef](#)]
95. Yang, B.; Liu, S.; Fedoseeva, Y.V.; Okotrub, A.V.; Makarova, A.A.; Jia, X.; Zhou, J. Engineering selenium-doped nitrogen-rich carbon nanosheets as anode materials for enhanced Na-Ion storage. *J. Power Sources* **2021**, *493*, 229700. [[CrossRef](#)]
96. Hao, R.; Yang, Y.; Wang, H.; Jia, B.; Ma, G.; Yu, D.; Guo, L.; Yang, S. Direct chitin conversion to N-doped amorphous carbon nanofibers for high-performing full sodium-ion batteries. *Nano Energy* **2018**, *45*, 220–228. [[CrossRef](#)]
97. Liu, H.; Jia, M.; Cao, B.; Chen, R.; Lv, X.; Tang, R.; Wu, F.; Xu, B. Nitrogen-doped carbon/graphene hybrid anode material for sodium-ion batteries with excellent rate capability. *J. Power Sources* **2016**, *319*, 195–201. [[CrossRef](#)]
98. Liu, S.; Yang, B.; Zhou, J.; Song, H. Nitrogen-rich carbon-onion-constructed nanosheets: An ultrafast and ultrastable dual anode material for sodium and potassium storage. *J. Mater. Chem. A* **2019**, *7*, 18499–18509. [[CrossRef](#)]
99. Qu, Y.; Guo, M.; Zeng, F.; Zou, C.; Yuan, C.; Zhang, X.; Li, Q.; Lu, H. Synthesis of nitrogen-doped porous carbon nanofibers as an anode material for high performance sodium-ion batteries. *Solid State Ion.* **2019**, *337*, 170–177. [[CrossRef](#)]
100. Lu, Y.; Li, D.; Lyu, C.; Liu, H.; Liu, B.; Lyu, S.; Rosenau, T.; Yang, D. High nitrogen doped carbon nanofiber aerogels for sodium ion batteries: Synergy of vacancy defects to boost sodium ion storage. *Appl. Surf. Sci.* **2019**, *496*, 143717. [[CrossRef](#)]
101. Sun, L.; Xie, J.; Zhang, X.; Zhang, L.; Wu, J.; Shao, R.; Jiang, R.; Jin, Z. Controllable synthesis of nitrogen-doped carbon nanobubbles to realize high-performance lithium and sodium storage. *Dalt. Trans.* **2020**, *49*, 15712–15717. [[CrossRef](#)]
102. Ding, K.; Gao, B.; Fu, J.; An, W.; Song, H.; Li, X.; Yuan, Q.; Zhang, X.; Huo, K.; Chu, P.K. Intertwined Nitrogen-Doped Carbon Nanotubes for High-Rate and Long-Life Sodium-Ion Battery.pdf. *ChemElectroChem* **2017**, *4*, 2542–2546. [[CrossRef](#)]
103. Bu, L.; Kuai, X.; Zhu, W.; Huang, X.; Tian, K.; Lu, H.; Zhao, J.; Gao, L. Nitrogen-doped double-shell hollow carbon spheres for fast and stable sodium ion storage. *Electrochim. Acta* **2020**, *356*, 136804. [[CrossRef](#)]
104. Khan, M.; Ahmad, N.; Lu, K.; Sun, Z.; Wei, C.; Zheng, X.; Yang, R. Nitrogen-doped carbon derived from onion waste as anode material for high performance sodium-ion battery. *Solid State Ion.* **2020**, *346*, 115223. [[CrossRef](#)]
105. Ou, J.; Yang, L.; Zhang, Z. Chrysanthemum derived hierarchically porous nitrogen-doped carbon as high performance anode material for Lithium/Sodium ion batteries. *Powder Technol.* **2019**, *344*, 89–95. [[CrossRef](#)]